1   **Revision 2**

2   **Melt-mediated re-equilibration of zircon produced during meltdown of the Chernobyl**

3   **reactor**

4   Denis Fougerouse[1,2]*, Thorsten Geisler[3], Steven M. Reddy[1,2], Matvei Aleshin[4], Laure Martin[4],

5   Luc S. Doucet[1], Zakaria Quadir[2], David Saxey[2] and William Rickard[2]

6   [1]School of Earth and Planetary Sciences, Curtin University, Perth, Australia

7   [2]Geoscience Atom Probe, Advanced Resource Characterisation Facility, John de Laeter

8   Centre, Curtin University, Perth, Australia

9   [3]Institute for Geosciences, University of Bonn, 53115 Bonn, Germany

10   [4]CMCA, University of Western Australia, Perth, Australia

11   *Corresponding author: Denis.fougerouse@curtin.edu.au

12

13   **Abstract**

14   The mineral zircon is used widely to constrain the age of rocks and the processes that

15   formed them. Although zircon is robust to a range of physical and chemical processes, it

16   may show evidence for rapid re-equilibration that is generally considered to reflect

17   interaction with hydrous fluids. Here, we show that zircon grains that crystallised from melt

18   produced during the catastrophic meltdown of the Chernobyl nuclear reactor exhibit re-

19   equilibration textures that occurred in an environment without free-water. The process of re-

20   equilibration involved a melt-mediated interface-coupled dissolution–reprecipitation that

21   took place over a few days to produce textures that are commonly observed in igneous and

22   anatectic systems. Thus, the composition of zircon can be modified even in the absence of

23   hydrous fluids in a short time-frame. Through this process, zircon crystals may track the

24   timing of the last silicate melt it interacted with.

25

26   **Introduction**

27   The catastrophic meltdown of the reactor 4 of the Chernobyl Nuclear Power Plant on April

28   26, 1986 is the worst nuclear disaster in history. The reactor experienced a suite of

29   unexpected events causing uncontrolled nuclear chain reaction (Mullner, 2019). The

30   temperature reached in excess of 2600°C causing the uranium fuel rods and their zirconium

31   alloy cladding to melt and drop at the bottom of the reactor (Burakov et al., 1996). This

32   molten material, or corium, dissolved constituents of the reactor including steel, concrete,

33   serpentine and sand, evolving to a silicate melt from which zircons [$ZrSiO_4$] crystallised at

34   temperature below 1250°C (Burakov et al., 1996; Pazukhin, 1994; Pöml et al., 2013; Ushakov

35   et al., 1996).

36   Zircon is a commonly used mineral to understand when and how rocks formed (Harley and

37   Kelly, 2007). Despite its chemical and physical robustness, the internal structure of zircon

38   grains can be chaotic and indicates that zircon may partially re-equilibrate in response to

39   changing pressure–temperature–composition (*P–T–X*) conditions (Martin et al., 2008;

40   Rubatto, 2017). To this day, hydrous fluids are believed to play an important role in

41   modifying particular domains within zircon, especially if they have been damaged by

42   radioactive decay (Geisler et al., 2003; Geisler et al., 2007). However, similar features are also

43   recorded in crystalline zircon grains from metamorphic environments (Rubatto et al., 2008)

44   or due to interaction with high-T magmatic fluids (Soman et al., 2010). Re-equilibration

45   textures in zircon have also been documented from a variety of settings in which hydrous

46   fluids likely played little or no role, including igneous (Bindeman and Melnik, 2016;

47   Gagnevin et al., 2010), high-grade metamorphic (Hoskin and Black, 2000; Zheng et al., 2004),

48   and experimental systems (Tomaschek, 2004). Although several mechanisms have been

49   proposed to drive reequilibration of zircon in fluid-deficient settings including solid-state

50   recrystallization (Hoskin and Black, 2000) and melt-mediated interface-coupled dissolution–

51   reprecipitation (Geisler et al., 2007), such mechanisms are poorly understood.

52   Chernobyl zircon grains, collected during an inspection of the Power Plant in 1989 are well

53   suited to study the re-equilibration of a crystalline zircon in an anhydrous melt (Shiryaev et

54   al., 2016). Although some of the Chernobyl melt interacted with water forming porous

55   ceramics in localised areas of the plant where water was pooling, the majority of the melt

56   was never in contact with water thanks to the rescue team that drained the flooded

57   basement, avoiding another, larger catastrophe. The Chernobyl melt remained at

58   atmospheric pressure during its evolution and therefore could only dissolve negligible

59   water (Carroll and Blank, 1997; Dixon et al., 1995; Silver et al., 1990). The Chernobyl zircons

60   contain high U contents, however they are virtually free of damage due to internal

61   radioactive decay. Here, we investigate the textural and chemical features of one of these

62   zircon grains using crystallographic orientation mapping, ion imaging, and nanoscale

63   analyses, with the aim of determining the mechanisms of zircon reequilibration in a dry

64   magmatic setting.

65

66   **Sample and methods**

67   At Chernobyl, several types of lava-like solidified materials have been described such as the

68   black and brown silicate glass as well as porous ceramics that formed by the interaction of

69   brown silicate melt with water (Burakov et al., 1996). The sample studied is a brown silicate

70   melt that was collected in the basement of the Chernobyl Power Plant (Borovoi, 2006).

71   Zircon grains were separated at the Khlopin Radium Institut in St. Petersburg by dissolving

72   the glass matrix in hydrofluoric acid. Secondary electron images did not reveal any signs of

73   zircon dissolution (Borovoi, 2006), and zircon grains separated without the use of

74   hydrofluoric acid have very similar textures to those reported here (Shiryaev et al., 2016).

75   Three zircon grains of a total weight of less than 0.4 mg were mounted in epoxy. The

76   radiometry measurements of the sample demonstrated relatively low activity with a dose

77   rate of about 0.25 microsieverts per hour (uSv/hr) at 5 cm from the sample. The activity of

78   the sample mount was estimated to be below 50 kBq. Radiometry measurements were

79   performed before and after the analysis to ensure that the fissile material was not lost during

80   the analysis. The sample does not contain particulate matter that could be easily lost.

81   Nevertheless, handling of the sample was carried out in controlled laminar hoods.

82   Scanning electron microscopy (SEM), focused ion beam (FIB) sample preparation,

83   transmission electron microscopy (TEM) and atom probe tomography (APT) analyses were

84   performed at the John de Laeter Centre, Curtin University. The sample was ion milled for 30

85   min at a 5° tilt using an Ar ion beam operated at a 5 kV accelerating voltage and a beam

86   current of 40 µA to remove the surface layer affected by mechanical polishing. Electron

87   backscattered imaging (BSE) and electron backscattered diffraction mapping (EBSD) were

88   performed on a Tescan Mira3 and Tescan Clara SEMs. The instruments were operated at 20

89   kV accelerating voltage and EBSD data was acquired with an Oxford Symmetry detector

90   and reduced with the Channel5 software. Samples for APT and TEM were prepared with a

91   Tescan Lyra3 Ga⁺ FIB-SEM. Pt fiducials deposited using an electron beam were used to

92   target the boundary between high- and low-U zircon (Rickard et al., 2020). The FIB was

93   operated at 30 kV during the manufacture of the APT and TEM specimens and at 2 kV to

94   remove the layer affected by high-energy Ga⁺ ion implantation. TEM analyses were

95   conducted on a FEI Talos FS200X FEG TEM operated at 200 kV in scanning mode (STEM)

96   and equipped with a Super-X EDS detector. We used the geoscience atom probe at Curtin

97   University for APT data collection (Reddy et al., 2020). The instrument (Cameca LEAP 4000X

98   HR) was used in laser pulsing mode with a UV laser (λ = 355 nm). The laser was pulsed at

99   125 kHz with a laser energy of 300 pJ and at an automated detection rate of 0.02 ion/pulse

100   and 60 K base temperature. The 3D reconstruction was performed using the Cameca IVAS

101   3.8 software using a voltage curve reconstruction and 32 V/nm evaporation field following a

102   standardised approach (Fougerouse et al., 2022; Saxey et al., 2019).

103   Scanning ion imaging was performed with a Cameca IMS 1280 equipped with Hyperion-II

104   radio-frequency oxygen ion source at the Centre for Microscopy, Characterisation and

105   Analysis, The University of Western Australia. Primary O_2^- ions were focused as a Gaussian

106   beam and accelerated by potential of -13 kV toward the sample under +10 kV and a bean

107   current was 70 pA. For uranium isotope analyses, ions on masses 234, 235, 236, 238 and 239

108   were detected simultaneously, and for plutonium analyses, ions on masses 238, 239, 240, 241

109   and 242 were measured. Since the IMS1280 magnet dispersion and minimal distance

110   between detectors do not allow to detect ions at such high masses simultaneously, the mass

111   dispersion was increased by using the stigmator (DSP2S1) located after the magnet. The

112   measurements were performed at a mass resolution of 2460 M/ΔM with an entrance slit of

113   200 μm, exit slit #1 (500 μm), a field aperture of 5000 μm and a contrast aperture of 400 μm.

114   Ion images are 50x50 μm in size and were processed using CAMECA SIMS Image

115   Processing Software WinImage II.

116

117   **Results**

118   **Textural relationships and isotopic composition of zircon domains**

119   The BSE images of the zircon grain reveal complex internal textures (Fig. 1). The grain

120   contains numerous inclusions of monoclinic $(Zr,U)O_2$ fuel fragments, and $(U,Zr)O_2$ that

121   crystallized early at high temperature from two immiscible melts that formed when the

122   nuclear fuel interacted with the zirconium alloy cladding (Burakov et al., 1996). The

123   brightest BSE response reflects highest U content in zircon (Geisler et al., 2005; Pöml et al.,

124   2013; Shiryaev et al., 2016). The high-U domains are truncated by lower-U curviplanar,

125   finger-like domains penetrating inward from the crystal margin (Fig. 1B). Low-U domains

126   are well developed in the external part of the grain and enclose numerous inclusions of

127    $(Zr,U)O_2$ and $(U,Zr)O_2$ that are apparently coarser than in the high-U domain. The grain

128   preserves remnants of primary oscillatory growth zoning, as well as faint ('ghost') zoning in

129   the low-U domains that mimics the overall grain shape and is consistent with primary

130   oscillatory zoning. A typical feature is the occurrence of micrometre-sized pores near or at

131   the interface between high- and low-U zircon domains (Fig. 1D; Fig. 1P in (Geisler et al.,

132   2007)). The pores at the interface are particularly common at high-curvature boundaries,

133   such as the tips of the finger-like domains (red arrows in Fig. 1D).

134   In the EBSD data, the colour variations on the texture component analysis are spatially

135   correlated with porosity and topographical features (Fig. 1C). No significant internal

136   deformation is evident, and the crystal orientation is continuous through the interface

137   between the high and low-U domains.

138   Ion imaging confirms that the ^{238}U abundance is high in the BSE bright, low in the dark

139   domains, and that the ^{240}Pu concentration mimics that of U (Fig. 2). The ^{235}U/^{238}U ratio map

140   and a profile across several finger-like features indicates that the uranium isotopic

141   composition is locally constant between high- and low-U domains (Fig. 2).

142   **Nanoscale observations**

143   The nanoscale analyses focused on the boundary between the high- and low-U domains of

144   the zircon grain (Fig. 3). The atom probe mass spectra are comparable with other APT

145   studies of zircon (Peterman et al., 2016; Saxey et al., 2018) despite well-developed U^{++}, UO^{++},

146   UO_2^+ and UO_2^{++} peaks (Fig. DR1). The APT measurements from the selected interface (Fig.

147   1E) show that the high-U zircon contains 1.1 at.% U and the low-U domains 0.6 at.% U. The

148   increase in U is compensated by a decrease in Zr, but not by a decrease in Si, as observed in

149   a previous electron microprobe study (Geisler et al., 2005). The boundary between the two

150   domains is sharp at the nanoscale, with the U concentration changing over ~7 nm (Fig. 3B).

151   No enrichment of trace elements is observed at the interface. Consistent with APT data, the

152   TEM observations in both the STEM bright field (BF) image and the STEM EDS map

153   indicates that the boundary between the two domains is discrete at the nanoscale (Fig. 3).

154   Small (~25 nm) ZrO_2 inclusions are also present in the high-U domains. The TEM data does

155   not reveal the presence of nanoscale porosity in either the high or low-U domains.

156   Consistent with the EBSD data, the crystal orientation is continuous across the boundary,

157   with no recognizable strain fields at the interface between the two domains.

158   **Discussion**

159   **Zircon growth and modification in silicate melt**

160   The incorporation of tetravalent ions in zircon (U, Pu and Th) creates lattice strain (Ewing,

161   1999; Finch and Hanchar, 2003; Meldrum et al., 1998; Ushakov et al., 1999). Ushakov et al.

162   (1999) determined the solubility of $USiO_4$ at 4 ± 1 at.% in zircon at 1500 °C. By applying Ti-

163   in-zircon thermometry (Ferry and Watson, 2007), the zircon crystals in the Chernobyl brown

164   glass likely crystallised at temperatures below 1250 °C (Pöml et al., 2013). These

165   temperatures are consistent with the stability of monoclinic ZrO_2 as observed in the core of

166   many zircon crystals from Chernobyl (Pöml et al., 2013).

167   In general, zircon crystals may become metastable under changing $P–T–X$ conditions and be

168   subjected to subsolidus modification (Rubatto, 2017). The finger-like low-U domains in the

169   zircons from the Chernobyl brown melt truncate primary oscillatory zoning, and in places

170   preserve remnants of it (Fig. 1 and 4). Similar embayment textures and 'ghost zoning'

171   whereby the primary oscillatory zoning affects the transient composition of the reaction

172   front have been attributed to re-equilibration (Black et al., 1986; Harley et al., 2007; Hoskin

173   and Black, 2000; Martin et al., 2008).

174   The composition of the Chernobyl glasses is variable and include some material that

175   interacted with water. However, the Chernobyl brown glass, from which the zircon studied

176   here has been extracted, is anhydrous within detection limits of Raman and reflectance

177   infrared spectroscopy (Shiryaev et al., 2016). As demonstrated experimentally, the water

178   solubility in silicate melts is negligible at atmospheric pressure (Carroll and Blank, 1997;

179   Dixon et al., 1995; Silver et al., 1990) and the Chernobyl silicate melt likely remained

180   anhydrous throughout its evolution. In anhydrous environment, three mechanisms have

181   been proposed to explain the observed textures: (1) dissolution of zircon in a melt followed

182   by epitaxial growth of compositionally-discrete zircon (Hibbard, 1981), (2) solid-state

183   recrystallization driven by the diffusion of REE defects (Hoskin and Black, 2000), and; (3)

184   melt-mediated interface-coupled dissolution–reprecipitation (Geisler et al., 2007).

185   The dissolution and growth model (1) is based on simple stability assumptions. In the

186   Chernobyl zircons, the U isotopic composition varies within single crystals and between

187   different zircon grains (Pöml et al., 2013). The $^{235}U/^{238}U$ composition of zircon crystals and

188   the inclusions they contains ranges from 0.0166 to 0.0088 and differs significantly from the

189   natural $^{235}U/^{238}U$ ratio of 0.007257 (Pöml et al., 2013). This can be explained by heterogeneous

190   mixing of melted uranium fuel rods that had different burnup and U isotopic composition

191   with theoretical $^{235}U/^{238}U$ value up to 0.02041 (for 2% ^{235}U enrichment) (Pöml et al., 2013). The

192   prediction from the dissolution and epitaxial growth model is that the primary and

193   secondary features should have different uranium isotope composition because of the

194   heterogeneous U isotopic composition of the brown melt. However, the $^{235}U/^{238}U$

195   composition across the different zircon domains is constant, and does not support this

196   model (Fig. 2).

197   The solid-state recrystallization model (2) is based on the slow diffusion of defects and REE

198   impurities that occur so as to reduce the lattice strain caused by impurities (Hoskin and

199   Black, 2000). Such process, is solely controlled by diffusion and is expected to produce

200   diffuse domains within zircon grains. However, the reaction front in the Chernobyl zircon is

201   sharp at the nanoscale (Fig. 3). The extremely low diffusion rate measured for U in

202   crystalline zircon (~10^{-25} m^2/s) at 1250 °C (Cherniak et al., 1997) means that, after ten days, U

203   would diffuse over a distance of ~0.4 nm. As such, the operation of a process controlled by

204   diffusion is extremely unlikely and the solid-state recrystallization driven by the diffusion of

205   REE defects (Hoskin and Black, 2000) is not supported by our data.

206   The textural relationship between primary and re-equilibrated zircon is also similar to that

207   created by aqueous-fluid-mediated interface-coupled dissolution–precipitation (Geisler et

208   al., 2007). Nanoscale investigations of the reaction front in fluid-mediated replacement

209   textures in ultra-high pressure zircons have revealed a network of nanoscale planar features

210   that are enriched and/or depleted in Y, Yb, U, and high-density clusters (< 10 nm) that are

211   enriched in Y, P, Yb, U, and Al (Peterman et al., 2019). In the Chernobyl zircon, trace element

212   segregation is not observed associated with either planar features or clusters and U is the

213   only element with a detectable change in concentration at the interface between both

214   domains.

215   The sharp gradient in U concentration, which can be interpreted as a boundary, supports the

216   idea that the low-U domains were formed by a process of surface-controlled and interface-

217   coupled dissolution-precipitation. During this process, the U-rich parent zircon dissolved in

218   the surrounding melt simultaneous with precipitation of new U-poor zircon along an

219   inwardly migrating reaction interface (Fig. 4). We hypothesize that the driving force for

220   migration of the interface was undersaturation of the surrounding melt with respect to U-

221   rich zircon due to changes in the global or local physicochemical conditions (Fig. 4). The

222   composition of the brown melt evolved with the progressive incorporation of basement

223   materials, including concrete, serpentine and sand (Pöml et al., 2013). Due to rapid changes

224   in the concentration of Zr and U in the melt, we postulate that the high-U zircon became

225   unstable (Fig. 4). Dissolution of the U-rich zircon caused the local melt to become

226   oversaturated in a U-poor zircon composition that eventually precipitated topotactically on

227   the dissolving zircon surface.

228   For such a process to operate, the formation of porosity in the product phase is critical for

229   mass transport from and to the reaction interface, where dissolution–precipitation reactions

230   take place (Geisler et al., 2019; Geisler et al., 2007; Putnis, 2002). Whereas no porosity was

231   observed at the nano-scale, micrometre-sized pores occur at the reaction interface,

232   particularly at the tips of the finger-like domains (Fig. 1). These pores are related to the

233   replacement process, but they are unlikely to form a connected network that could have

234   provided continuous pathways for melt to reach the reaction interface.

235   We interpret the large pores at the tips of the secondary low-U domains to represent the

236   final products of coarsening of fine-scale porosity formed during the replacement process by

237   pore ripening processes, as suggested to explain missing interconnected porosity in fluid-

238   mediated replacement reactions (Fougerouse et al., 2016; Putnis, 2002; Vonlanthen et al.,

239   2012). Porosity must have been created during the replacement process by the molar volume

240   and solubility difference between the parent and product zircon (Geisler et al., 2007).

241   Thermodynamically, such a ripening process is driven by the reduction in surface area,

242   comparable to crack healing within a single crystal (Brantley et al., 1990).

243   Although numerous inclusions are present in the grain, these inclusions can be observed in

244   both primary and secondary domains and are unlikely to be entirely the result of the re-

245   equilibration as opposed to the process described during fluid-mediated interface-coupled

246   dissolution–precipitation (Geisler et al., 2007; Soman et al., 2010). Notably, the mineral

247   inclusions of ZrO_2 and UO_2 are coarser in the re-equilibrated domains (Fig. 1). This

248   observation suggests that these inclusions may have grown during replacement (Fig. 4). The

249   observed chemical variation between the re-equilibrated and primary zircon is significant

250   (>0.5 at.% U), but the variability is much larger in other crystals (Geisler et al., 2005; Shiryaev

251   et al., 2020). The excess U that is released from the primary zircon during its replacement

252   could be the source for coarsening of UO_2 inclusions. If true, this requires pathways for U to

253   be transported away from the reaction front.

254   **Geological implications**

255   Core–rim textures similar to those observed in the Chernobyl zircon have been described

256   from various geological systems. In magmatic systems, "patchy textures" have been

257   reported from felsic rhyolite and A-type granite (Breiter et al., 2014), monzogranite

258   (Bindeman and Simakin, 2014; Gagnevin et al., 2010) and granodiorite (Wang et al., 2002). In

259   every instance, high-U–Th–Y zircon cores were replaced by low-U–Th–Y domains that have

260   (where measured) Th/U ratios below 0.1. Magma mixing is generally accepted as the main

261   mechanism by which the melt composition is changed, which acts as the driving force for

262   replacement (Bindeman and Simakin, 2014; Gagnevin et al., 2010). Bindeman and Simakin

263   (2014) suggest that the Zr-saturation of the magma is the principal cause of reaction,

264   whereas the preferred model of Gagnevin et al. (2010) is the mixing of a metaluminous melt

265   in a peraluminous system, in which co-crystallisation of phosphate with zircon explains the

266   formation of secondary low-U–Th–Y replacement zones. A melt-mediated interface-coupled

267   dissolution-reprecipitation provides a mechanism that is able to explain replacement

268   textures that form under dry conditions.

269   The model commonly used to explain zircon re-equilibration textures is that they formed via

270   solid-solution recrystallization and diffusion of defects (Hoskin and Black, 2000). Such a

271   process, is expected to produce diffuse domains but is inconsistent with the sharp interface

272   between parent zircon and re-equilibrated low-U–Th–Y domains observed in high-grade

273   metamorphic rocks (Chen et al., 2013; Dong et al., 2017). Therefore, we propose that, during

274   interactions with silicate melts, melt-mediated coupled dissolution-reprecipitation

275   mechanism is an effective mechanism for zircon re-equilibration that produce a sharp

276   interface between the parent zircon and the re-equilibrated low-U–Th–Y domains. As Pb is

277   not incorporated in the zircon crystal lattice during crystallisation, we postulate that Pb is

278   expelled during melt-driven interface-coupled dissolution-reprecipitation, thereby resetting

279   the U–Th–Pb geochronometer. Thus, in case of metamorphic resetting, either the entire grain

280   or low-U–Th–Y domains (rim) of zircons may record the timing of onset of anatexis rather

281   than peak metamorphism as suggested by melt-mediated monazite experiments (Varga et

282   al., 2020). Although Chernobyl zircons have extraordinarily high-U content and could be

283   particularly reactive, this process may occur rapidly over a few days, and may record only

284   small degrees of melt–zircon interactions. Melt-driven interface-coupled dissolution-

285   reprecipitation should be considered as an age resetting mechanism when retracing *P–T*

286   metamorphic paths in high-grade metamorphic rocks. Such mechanism may also be

287   important during magma mixing in magmatic chambers, late-stage magmatism during

288   orogenic events and zircon recycling. It has been documented that there is a preservation

289   bias of high-U zircons in the detrital zircon record due to metamictisation and weathering

290   (Dröllner et al., 2022; Markwitz and Kirkland, 2018; Resentini et al., 2020). This study

291   suggests that melt-mediated re-equilibration is another process that can induce a

292   preservation bias of high-U zircons record, in particular if the recycling process is mediated

293   by a silicate melt. Although the Chernobyl zircon crystal are likely more reactive than

294   natural zircons, re-equilibration textures observed in a range of felsic rocks as detailed above

295   suggest that this process may be active during continental crust recycling. In addition, as Hf

296   is incorporated as a structural element in zircon (Kinny and Maas, 2003), we postulate that

297   re-equilibration of high-U zircon should preserve original Lu/Hf and Hf isotope ratios. This

298   hypothesis seems reasonable considering that metamorphic zircons preserve their

299   initial $^{176}Hf/^{177}Hf$ ratio and have comparable or lower Lu/Hf ratios compared to igneous

300   zircons (Hoskin and Black, 2000; Kinny and Maas, 2003). However, because the U–Th–Pb

301   geochronometer may be reset, it can lead to underestimate the Hf isotope composition of the

302   source. It is unclear how such bias is expressed in the detrital record for example, but

303   indicates that zircon re-equilibration texture must be considered for Lu/Hf studies.

304

305   Conclusions

306   This research presents microstructural, isotopic and nanoscale information of a complex

307   zircon crystal to yield unique insight into the mechanism of mineral re-equilibration in the

308   absence of water. The data show that re-equilibration likely operates through a surface-

309   controlled and interface-coupled reaction process of dissolution and reprecipitation

310   mediated by a silicate melt. The U-rich zircon dissolves and U-poor zircon simultaneously

311   precipitates following a reaction front penetrating in the zircon crystal. The reaction

312   occurred rapidly (<2 weeks) and is likely driven by the instability of high-U zircon after

313   changes in the parent melt composition and the assimilation of material from the nuclear

314   plant. The melt-mediated dissolution-reprecipitation process is likely to be common in

315   natural contexts, including but not limited to, anataxis, magma mixing, late-stage

316   magmatism during orogenic events and zircon recycling. In all cases, the geological record

317   of inherited, U-rich zircons may be lost through mineral re-equilibration.

318   **Acknowledgments**

327

328   **Figure caption**

329   **Figure 1: Grain-scale textural analysis of a zircon grain from the Chernobyl "lava".** A) BSE

330   image; B) Contrast enhanced BSE image. The bright inclusions are a mix of UO_2 and ZrO_2.

331   The shades of grey indicate a higher average atomic weight and correspond to the U

332   content. Low-U zircon replaces high-U zircon along inward penetrating embayments. The

333   primary oscillatory zoning is truncated but ghost zoning remains present in the low-U

334   zircon; C) Crystallographic orientation electron backscattered diffraction (EBSD) map.

335   Misorientation is colour coded from reference point "+" to maximum of 10°. No variation in

336   crystal orientation can be observed between the low- and high-U domains; D) BSE image

337   enhancement of the zircon core. The red arrows point to the finger-like embayments; B)

338   Close up of the region of interest with the atom probe tomography (APT) and transmission

339   electron microscopy (TEM) specimens location indicated.

340   **Figure 2: Ion imaging of secondary textures.** A) ^{238}U counts maps showing high and low-U

341   zircon domains and bright UO_2 inclusions; B) $^{235}U/^{238}U$ ratio map indicating that the zircon U

342   isotopic composition is locally homogeneous across all domains; C) line profile (indicated in

343   B) illustrating the ^{238}U, ^{240}Pu and $^{235}U/^{238}U$ composition of the primary and secondary

344   domains.

345   **Figure 3: Nanoscale analyses.** A) Atom probe 3D reconstruction of the APT specimen. Each

346   purple dot represents a single U atom. The U distribution is heterogeneous with a high-U

347   and a low-U domain separated by a sharp boundary; B) Chemical profile across the

348   boundary from the APT data. The location of the profile is indicated on A. The U content

349   varies by ~0.5 at.% over <7 nm; C) STEM BF image across the reaction. No nanoscale

350   porosity is present in the re-equilibrated zircon; D) STEM EDS map for U confirms the sharp

351   nature of the reaction front.

352   **Figure 4: Interpretative schematic diagram of the zircon history.** Left) The zircon grows in

353   equilibrium with high-U melt with strong primary zoning and numerous inclusions;

354   Middle) the re-equilibration to low-U zircon first occurs along grain boundaries. The

355   inclusions coarsen during the dissolution-reprecipitation reaction; Right) the re-equilibration

356   becomes pervasive throughout the grain with the development of large porosity and large

357   inclusions. The primary zoning is truncated by the low-U zircon, but some primary zoning

358   is faintly preserved as ghost zoning.

359   **References**

360 Bindeman, I. and Simakin, A. (2014) Rhyolites—Hard to produce, but easy to recycle and

361 sequester: Integrating microgeochemical observations and numerical models. Geosphere 10,

362 930-957.

363 Bindeman, I.N. and Melnik, O.E. (2016) Zircon survival, rebirth and recycling during crustal

364 melting, magma crystallization, and mixing based on numerical modelling. Journal of

365 Petrology 57, 437-460.

366 Black, L., Williams, I. and Compston, W. (1986) Four zircon ages from one rock: the history

367 of a 3930 Ma-old granulite from Mount Sones, Enderby Land, Antarctica. Contributions to

368 Mineralogy and Petrology 94, 427-437.

369 Borovoi, A. (2006) Database for the model of lava generation and spreading. Tech. Rep.

370 Project ''Chess'', 2916.

371 Brantley, S.L., Evans, B., Hickman, S.H. and Crerar, D.A. (1990) Healing of microcracks in

372 quartz: Implications for fluid flow. Geology 18, 136-139.

373 Breiter, K., Lamarão, C.N., Borges, R.M.K. and Dall'Agnol, R. (2014) Chemical characteristics

374 of zircon from A-type granites and comparison to zircon of S-type granites. Lithos 192, 208-

375 225.

376 Burakov, B., Anderson, E., Shabalev, S., Strykanova, E., Ushakov, S., Trotabas, M., Blanc, J.,

377 Winter, P. and Duco, J. (1996) The behavior of nuclear fuel in first days of the Chernobyl

378 accident. MRS Online Proceedings Library (OPL) 465.

379 Carroll, M.R. and Blank, J.G. (1997) The solubility of H2 O in phonolitic melts. American

380 Mineralogist 82, 549-556.

381 Chen, Y.X., Zheng, Y.F. and Hu, Z. (2013) Petrological and zircon evidence for anatexis of

382 UHP quartzite during continental collision in the Sulu orogen. Journal of Metamorphic

383 Geology 31, 389-413.

384   Cherniak, D.J., Hanchar, J.M. and Watson, E.B. (1997) Diffusion of tetravalent cations in

385   zircon. Contributions to Mineralogy and Petrology 127, 383-390.

386   Dixon, J.E., Stolper, E.M. and Holloway, J.R. (1995) An experimental study of water and

387   carbon dioxide solubilities in mid-ocean ridge basaltic liquids. Part I: calibration and

388   solubility models. Journal of Petrology 36, 1607-1631.

389   Dong, C., Xie, H., Kröner, A., Wang, S., Liu, S., Xie, S., Song, Z., Ma, M., Liu, D. and Wan, Y.

390   (2017) The complexities of zircon crystllazition and overprinting during metamorphism and

391   anatexis: an example from the late Archean TTG terrane of western Shandong Province,

392   China. Precambrian Research 300, 181-200.

393   Dröllner, M., Barham, M. and Kirkland, C.L. (2022) Gaining from loss: Detrital zircon source-

394   normalized α-dose discriminates first-versus multi-cycle grain histories. Earth and Planetary

395   Science Letters 579, 117346.

396   Ewing, R.C. (1999) Nuclear waste forms for actinides. Proceedings of the National Academy

397   of Sciences 96, 3432-3439.

398   Ferry, J. and Watson, E. (2007) New thermodynamic models and revised calibrations for the

399   Ti-in-zircon and Zr-in-rutile thermometers. Contributions to Mineralogy and Petrology 154,

400   429-437.

401   Finch, R.J. and Hanchar, J.M. (2003) Structure and chemistry of zircon and zircon-group

402   minerals. Reviews in mineralogy and geochemistry 53, 1-25.

403   Fougerouse, D., Micklethwaite, S., Tomkins, A.G., Mei, Y., Kilburn, M., Guagliardo, P.,

404   Fisher, L.A., Halfpenny, A., Gee, M. and Paterson, D. (2016) Gold remobilisation and

405   formation of high grade ore shoots driven by dissolution-reprecipitation replacement and Ni

406   substitution into auriferous arsenopyrite. Geochimica et Cosmochimica Acta 178, 143-159.

407   Fougerouse, D., Saxey, D.W., Rickard, W.D.A., Reddy, S.M. and Verberne, R. (2022)

408   Standardizing Spatial Reconstruction Parameters for the Atom Probe Analysis of Common

409   Minerals. Microscopy and Microanalysis 28, 1221-1230.

410   Gagnevin, D., Daly, J.S. and Kronz, A. (2010) Zircon texture and chemical composition as a

411   guide to magmatic processes and mixing in a granitic environment and coeval volcanic

412   system. Contributions to Mineralogy and Petrology 159, 579-596.

413   Geisler, T., Burakov, B.E., Zirlin, V., Nikolaeva, L. and Pöml, P. (2005) A Raman

414   spectroscopic study of high-uranium zircon from the Chernobyl. European Journal of

415   Mineralogy 17, 883-894.

416   Geisler, T., Dohmen, L., Lenting, C. and Fritzsche, M.B. (2019) Real-time in situ observations

417   of reaction and transport phenomena during silicate glass corrosion by fluid-cell Raman

418   spectroscopy. Nature materials 18, 342-348.

419   Geisler, T., Pidgeon, R.T., Kurtz, R., Van Bronswijk, W. and Schleicher, H. (2003)

420   Experimental hydrothermal alteration of partially metamict zircon. American Mineralogist

421   88, 1496-1513.

422   Geisler, T., Schaltegger, U. and Tomaschek, F. (2007) Re-equilibration of zircon in aqueous

423   fluids and melts. Elements 3, 43-50.

424   Harley, S.L. and Kelly, N.M. (2007) Zircon tiny but timely. Elements 3, 13-18.

425   Harley, S.L., Kelly, N.M. and Möller, A. (2007) Zircon behaviour and the thermal histories of

426   mountain chains. Elements 3, 25-30.

427   Hibbard, M. (1981) The magma mixing origin of mantled feldspars. Contributions to

428   Mineralogy and Petrology 76, 158-170.

429   Hoskin, P. and Black, L. (2000) Metamorphic zircon formation by solid-state recrystallization

430   of protolith igneous zircon. Journal of metamorphic Geology 18, 423-439.

431   Kinny, P.D. and Maas, R. (2003) Lu–Hf and Sm–Nd isotope systems in zircon. Reviews in

432   mineralogy and geochemistry 53, 327-341.

433   Markwitz, V. and Kirkland, C. (2018) Source to sink zircon grain shape: Constraints on

434   selective preservation and significance for Western Australian Proterozoic basin provenance.

435   Geoscience Frontiers 9, 415-430.

436   Martin, L.A., Duchêne, S., Deloule, E. and Vanderhaeghe, O. (2008) Mobility of trace

437   elements and oxygen in zircon during metamorphism: consequences for geochemical

438   tracing. Earth and Planetary Science Letters 267, 161-174.

439   Meldrum, A., Zinkle, S., Boatner, L. and Ewing, R.C. (1998) A transient liquid-like phase in

440   the displacement cascades of zircon, hafnon and thorite. Nature 395, 56-58.

441   Mullner, N. (2019) Three Decades after Chernobyl: Technical or Human Causes?, The

442   Technological and Economic Future of Nuclear Power. Springer VS, Wiesbaden, pp. 323-340.

443   Pazukhin, E. (1994) Fuel-containing lavas of the Chernobyl NPP fourth block: topography,

444   physicochemical properties, and formation scenario. Radiochemistry 36.

445   Peterman, E., Reddy, S.M., Saxey, D., Fougerouse, D., Snoeyenbos, D. and Rickard, W. (2019)

446   Nanoscale processes of trace element mobility in metamorphosed zircon. Contributions to

447   Mineralogy and Petrology 174, 92.

448   Peterman, E.M., Reddy, S.M., Saxey, D.W., Snoeyenbos, D.R., Rickard, W.D., Fougerouse, D.

449   and Kylander-Clark, A.R. (2016) Nanogeochronology of discordant zircon measured by

450   atom probe microscopy of Pb-enriched dislocation loops. Science Advances 2, e1601318.

451   Pöml, P., Burakov, B., Geisler, T., Walker, C., Grange, M., Nemchin, A., Berndt, J., Fonseca,

452   R., Bottomley, P. and Hasnaoui, R. (2013) Micro-analytical uranium isotope and chemical

453   investigations of zircon crystals from the Chernobyl "lava" and their nuclear fuel inclusions.

454   Journal of nuclear materials 439, 51-56.

455   Putnis, A. (2002) Mineral replacement reactions: from macroscopic observations to

456   microscopic mechanisms. Mineralogical Magazine 66, 689-708.

457   Reddy, S.M., Saxey, D.W., Rickard, W.D.A., Fougerouse, D., Montalvo, S.D., Verberne, R.

458   and van Riessen, A. (2020) Atom Probe Tomography: Development and Application to the

459   Geosciences. Geostandards and Geoanalytical Research n/a.

460   Resentini, A., Andò, S., Garzanti, E., Malusà, M.G., Pastore, G., Vermeesch, P., Chanvry, E.

461   and Dall'Asta, M. (2020) Zircon as a provenance tracer: Coupling Raman spectroscopy and

462   UPb geochronology in source-to-sink studies. Chemical Geology 555, 119828.

463   Rickard, W.D.A., Reddy, S.M., Saxey, D.W., Fougerouse, D., Daly, L., Peterman, E., Timms,

464   N., Cavosie, A.J. and Jourdan, F. (2020) Novel Applications of FIB-based Techniques in

465   Atom Probe Tomography Workflows. Microscopy and Microanalysis.

466   Rubatto, D. (2017) Zircon: the metamorphic mineral. Reviews in mineralogy and

467   geochemistry 83, 261-295.

468   Rubatto, D., Müntener, O., Barnhoorn, A. and Gregory, C. (2008) Dissolution-reprecipitation

469   of zircon at low-temperature, high-pressure conditions (Lanzo Massif, Italy). American

470   Mineralogist 93, 1519-1529.

471   Saxey, D., Fougerouse, D., Rickard, W. and Reddy, S. (2019) Spatial Reconstruction of Atom

472   Probe Data from Zircon. Microscopy and Microanalysis 25, 2536-2537.

473   Saxey, D., Reddy, S.M., Fougerouse, D. and Rickard, W.D. (2018) The Optimization of Zircon

474   Analyses by Laser-Assisted Atom Probe Microscopy: Insights from the 91500 Zircon

475   Standard. Microstructural Geochronology: Planetary Records Down to Atom Scale, 293-313.

476   Shiryaev, A.A., Burakov, B.E., Vlasova, I.E., Nickolsky, M.S., Averin, A.A. and Pakhnevich,

477   A.V. (2020) Study of mineral grains extracted from the Chernobyl "lava". Mineralogy and

478   Petrology 114, 489-499.

479   Shiryaev, A.A., Vlasova, I.E., Burakov, B.E., Ogorodnikov, B.I., Yapaskurt, V.O., Averin,

480   A.A., Pakhnevich, A.V. and Zubavichus, Y.V. (2016) Physico-chemical properties of

481   Chernobyl lava and their destruction products. Progress in Nuclear Energy 92, 104-118.

482   Silver, L.A., Ihinger, P.D. and Stolper, E. (1990) The influence of bulk composition on the

483   speciation of water in silicate glasses. Contributions to mineralogy and petrology 104, 142-

484   162.

485   Soman, A., Geisler, T., Tomaschek, F., Grange, M. and Berndt, J. (2010) Alteration of

486   crystalline zircon solid solutions: a case study on zircon from an alkaline pegmatite from

487   Zomba–Malosa, Malawi. Contributions to Mineralogy and Petrology 160, 909-930.

488   Tomaschek, F. (2004) Zircon reequilibration by dissolution–reprecipitation: reaction textures

489   from flux-grown solid solutions. Beihefte zum Eur J Mineral 12, 214.

490   Ushakov, S., Burakov, B., Shabalev, S. and Anderson, E. (1996) Interaction of UO2 and

491   zircaloy during the Chernobyl accident. MRS Online Proceedings Library (OPL) 465.

492   Ushakov, S., Gong, W., Yagovkina, M., Helean, K., Lutze, W. and Ewing, R. (1999) Solid

493   solutions of Ce, U, and Th in zircon. Ceramic Transactions 93, 357-364.

494   Varga, J., Raimondo, T., Daczko, N.R. and Adam, J. (2020) Experimental alteration of

495   monazite in granitic melt: Variable U–Th–Pb and REE mobility during melt-mediated

496   coupled dissolution-precipitation. Chemical Geology 544, 119602.

497   Vonlanthen, P., Fitz Gerald, J.D., Rubatto, D. and Hermann, J. (2012) Recrystallization rims

498   in zircon (Valle d'Arbedo, Switzerland): An integrated cathodoluminescence, LA-ICP-MS,

499   SHRIMP, and TEM study. American Mineralogist 97, 369-377.

500   Wang, X., Griffin, W., O'reilly, S., Zhou, X., Xu, X., Jackson, S. and Pearson, N. (2002)

501   Morphology and geochemistry of zircons from late Mesozoic igneous complexes in coastal

502   SE China: implications for petrogenesis. Mineralogical Magazine 66, 235-251.

503   Zheng, Y.-F., Wu, Y.-B., Chen, F.-K., Gong, B., Li, L. and Zhao, Z.-F. (2004) Zircon U-Pb and

504   oxygen isotope evidence for a large-scale 18O depletion event in igneous rocks during the

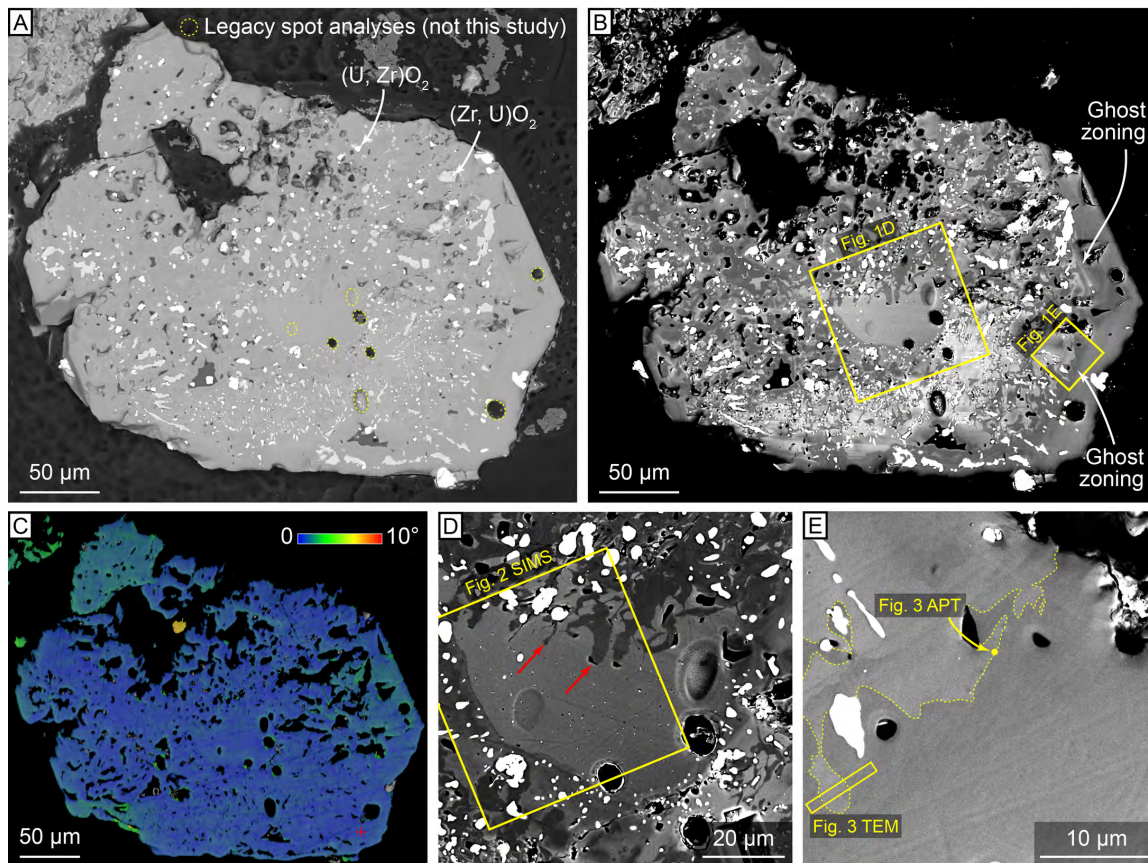505   Neoproterozoic. Geochimica et Cosmochimica Acta 68, 4145-4165.

506

Figure 1

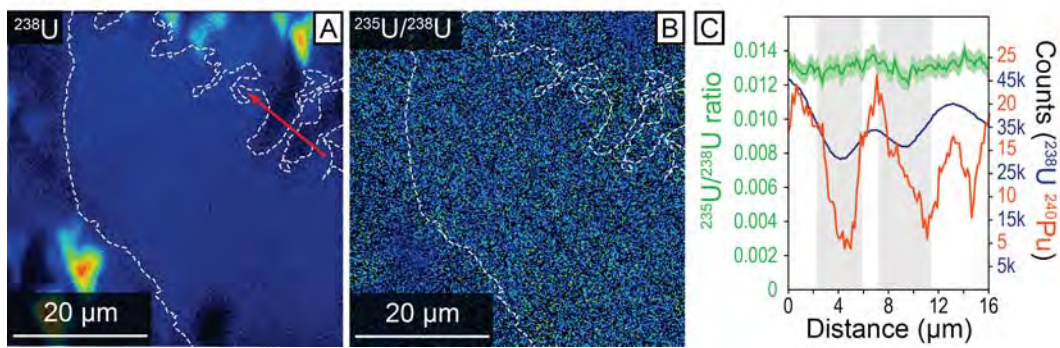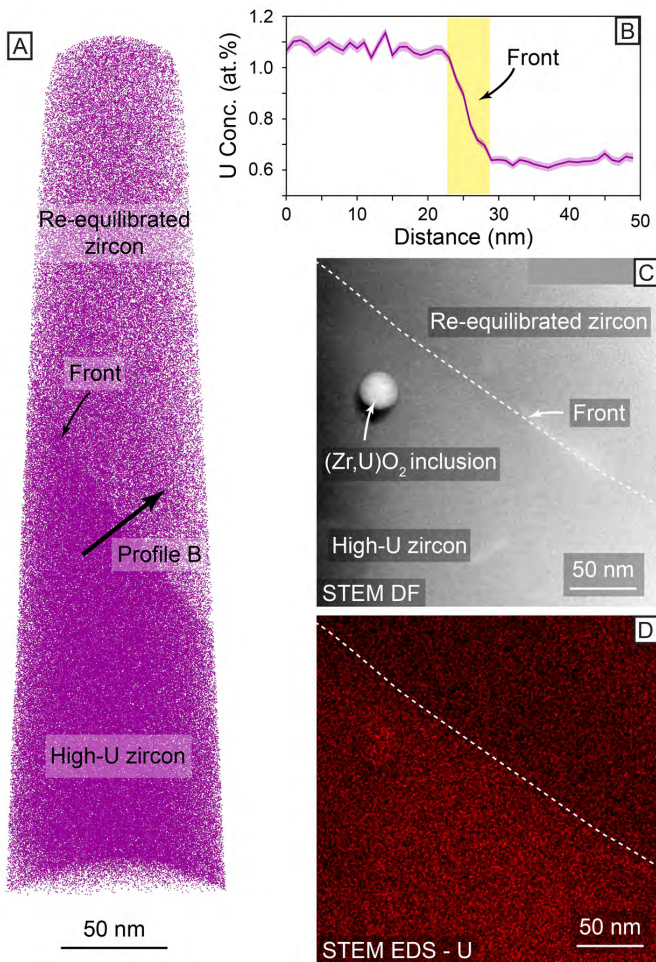A — Legacy spot analyses (not this study); (U, Zr)O$_2$; (Zr, U)O$_2$; 50 μm

B — Ghost zoning; Fig. 1D; Fig. 1E; Ghost zoning; 50 μm

C — 0 — 10°; 50 μm

D — Fig. 2 SIMS; 20 μm

E — Fig. 3 APT; Fig. 3 TEM; 10 μm

Figure 2

Figure 3

A

Re-equilibrated zircon

Front

Profile B

High-U zircon

50 nm

B

Front

C

Re-equilibrated zircon

Front

(Zr,U)O₂ inclusion

High-U zircon

STEM DF

50 nm

D

STEM EDS - U

50 nm

Figure 4